Evolution of the microstructure of a 15-5PH martensitic stainless steel during precipitation hardening heat treatment

Laurent Couturier, Frederic de Geuser, Marion Descoins, Alexis Deschamps

Effect of the precipitation hardening treatment on the microstructure of a 15-5 PH martensitic stainless steel

Laurent Couturier[1,2,3], Frédéric De Geuser[1,2], Marion Descoins[4], Alexis Deschamps[1,2]

[1] Univ. Grenoble Alpes, SIMAP, F-38000 Grenoble, France
[2] CNRS, SIMAP, F-38000 Grenoble, France
[3] Department of Materials Engineering, the University of British Columbia, Vancouver, BC, Canada V6T 1Z4
[4] Aix-Marseille Université, CNRS, IM2NP UMR 7334, Campus de Saint-Jérôme, Avenue Escadrille Normandie Niemen, Case 142, F-13397 Marseille, France

Corresponding author: Laurent Couturier, laurent.couturier@ubc.ca

Abstract

The mechanical properties of precipitation-hardened stainless steels rely on a complex multi-scale microstructure developed during a sequence of quenching from austenitization, followed by a precipitation heat treatment. Important features of the resulting microstructure include the microstructure of martensite, retained and reverted austenite, nanoscale precipitation and the homogeneity of the Cr concentration. In this paper, the microstructure of a Cu-bearing 15-5PH steel is thoroughly characterized along the precipitation heat treatment, using a combination of transmission electron microscopy with phase and orientation mapping, atom probe tomography, in-situ small-angle X-ray scattering and X-ray diffraction. The fraction of austenite is observed to increase during the ageing treatment, together with the precipitation of the Cu precipitates, which present a core-shell structure with a shell enriched in Ni, Mn and Si. After heat treatment, the Cr concentration is found to be slightly inhomogeneous in the matrix, with in addition some significant segregation at the dislocations.

Highlights

- The multi-scale microstructure is characterized along precipitation heat treatment
- Austenite reverts during precipitation treatment
- Cu precipitates form with a core-shell structure with a Ni, Mn, Si enriched shell
- Cr segregates on dislocations during heat treatment

Keywords

Stainless steel ; Cu precipitation ; atom probe tomography ; small-angle X-ray scattering ; automated crystal orientation mapping

1 Introduction

Precipitation hardened stainless steels are used for a wide range of applications requiring the combination of high strength, good toughness and corrosion resistance [1]. In most cases their process route involves the formation of a martensitic microstructure during a quench from the austenite field, followed by an ageing treatment where precipitation occurs. Depending on the alloy, this precipitation involves most classically Cu, such as in the 15-5PH or 17-4PH alloys, NiAl such as in the 13-8PH alloy or even $Ni_3(Mo,Ti)$. Tailoring the characteristics of this precipitation in terms of volume fraction and size allows adjusting the balance of the steel in terms of yield strength (or ultimate tensile strength) and fracture toughness [2]. Thus, the Cu precipitation sequence in Fe based alloys [1,3–5] and its impact on mechanical properties of PH stainless steels 17-4PH and 15-5PH [6–10] has been thoroughly investigated during the last decades.

However, the microstructure of a steel such as the 15-5 PH at the end of the precipitation ageing treatment is very complex, involving features at different scales, that depend on each step of the thermal history, which can each have determining influences on the materials' properties and on their subsequent evolution during in-service ageing:

- The martensitic structure inherited from the quench may evolve during the ageing treatment, with modifications of the dislocation density and/or lath structure
- The alloy is not 100% martensitic and austenite may be present after the quench (retained austenite) as well as develop during the ageing treatment (reverted austenite) [11,12]. In the latter case, there can be complex solute partitioning and interaction with the other microstructural features
- Precipitation of Cu can interact with the other solutes present in the material such as Ni, Mn, Si: these elements may be partitioned during the formation of the precipitates and therefore influence their formation
- The presence of other precipitates such as carbides is also of interest
- The Fe-Cr solid solution may not be entirely homogeneous at the end of the ageing treatment

The present contribution aims at determining the role of the ageing treatment on the development of these different microstructural features through a multi-scale characterization procedure carried out both in the as-quenched state and during, or after the ageing treatment. The grain structure will be evaluated at fine scale using automated crystal orientation mapping (ACOM) in the transmission electron microscope (TEM). In addition, the fraction of austenite will be evaluated by X-ray diffraction (XRD). The precipitate microstructure will be evaluated in-situ during the ageing treatment using small-angle X-ray scattering (SAXS), supported by TEM. Atom probe tomography (APT) will be used to evaluate the distribution of chemical species in the precipitates and in their vicinity, as well as to evaluate the distribution of Cr atoms in the matrix, and in a particular case to determine the partitioning between austenite and martensite.

2 Material and experimental methods

The material used in this study is part of an industrial casting, supplied by the company Aubert&Duval, which composition range is given in Table 1. The major alloying elements are chromium, nickel and copper but it also contains lower amounts of silicon and manganese, niobium and molybdenum and very low carbon. After its solidification, the steel has been forged, homogenized at 1040°C, air quenched and finally tempered at 505°C giving rise to

precipitation hardening. In this study, we have at our disposal the material both in the air quenched and precipitation hardened conditions.

For optical microscopy observations, the samples were electrochemically etched using a solution of hydrofluoric acid diluted in water (15%) with a tension of 15V.

XRD experiments were conducted on a PANalytical X'PERT MPD apparatus equipped with a 1D detector, using a cobalt source (wavelength 1.789Å) on samples with very low roughness (final polishing with alumina 0.04µm) to increase the separation of the (110) martensite and (111) austenite peaks. The austenite volume fraction f_γ was then determined in comparing the intensity of these two peaks, respectively I_α and I_γ, according to the method proposed by Tanaka and Choi [13]:

$$f_\gamma = \frac{{R_\alpha}/{R_\gamma}\, I_\gamma}{I_\alpha + {R_\alpha}/{R_\gamma}\, I_\gamma} \quad (1)$$

$$R = \frac{F^2 P L e^{-2M}}{a^6} \quad (2)$$

with a the lattice parameter, F the structural factor of the considered crystalline planes, P the multiplicity factor, L the Lorentz polarization factor and e^{-2M} the temperature factor (numerical values in Table 2). In the present case the ratio ${R_\alpha}/{R_\gamma}$ is equal to 1.28.

For SAXS experiments, 300µm sheet samples were cut from the bulk material and thinned down to 40µm ±20µm by mechanical polishing. The experiments were conducted at the European Synchrotron Research Facility (ESRF) on the BM02-D2AM beamline using an X-Ray energy of 5.983 keV and a 2D-CCD camera. The images obtained from the CCD camera were then corrected for electronic noise, spatial distortion, pixels efficiency and background noise. All the corrected images were azimuthally averaged in order to obtain the scattered intensity as a function of the scattering vector amplitude ranging from $3x10^{-2}Å^{-1}$ to $6x10^{-1}Å^{-1}$ in the present case. The scattered intensity was converted to absolute measurement using a reference amorphous carbon sample [14]. In-situ measurements were carried out during the ageing treatment in a custom-built furnace allowing for transmission SAXS measurements.

TEM samples were cut from the bulk material in the precipitate hardened condition, thinned down to 80µm using mechanical polishing, and then cut in 3mm disks and electropolished using a double jet TenuPol 5 with a mixture of 10% perchloric acid, 20% 2-butoxyethanol and ethanol at 2°C under 14V voltage. The experiments were conducted on a Jeol 3100 instrument, both in conventional imaging mode and in scanning mode with a continuous recording of diffraction patterns for ACOM measurements using the ASTAR software, allowing us to obtain crystallographic orientations and phases maps of a selected area of material [15].

APT experiments were conducted on a LEAP 3000X HR instrument. Samples of dimensions $0.2x0.2x15mm^3$ were cut from the bulk material and prepared according to the two-step polishing procedure described in [16] using first a mixture of 5% perchloric acid in acetic acid and then a mixture of 2% perchloric acid in 2-butoxyethanol with a voltage varying from 25V to 5V. APT measurements were carried out using the laser mode (wavelength 532nm) of the LEAP instrument with an energy varying from 0.6nJ to 0.2nJ and an evaporation rate up to 1% at a temperature of 40K.

3 Results and discussions

3.1 Microstructure of martensite

After homogenization treatment at 1040°C, the material microstructure is fully austenitic with equiaxed grains of diameter approximately 20 µm. The austenite undergoes a martensitic transformation during the subsequent quench giving rise to the formation of lath martensite inside the former austenite grains. This martensitic structure is still present after the precipitation treatment (Figure 1). It is body centered cubic, due to its very low carbon content, with a lattice parameter measured by XRD of 2.87Å. The martensitic microstructure is characterized in more detail using ACOM imaging in the TEM, as shown in Figure 2. The phase maps (Fig. 2(a) and (c)) show that the material is essentially martensitic, but also highlight zones of austenite. The orientation maps in Figure 2(b) and (d) show the presence of the laths of a few µm separated by high angle grain boundaries. Within the laths, the crystal orientation is observed to vary continuously (Figure 2(e)) which is typical for the presence of a high dislocation density characteristic of martensite [17], and retained after the ageing treatment.

3.2 Austenite

As demonstrated by the phase maps of Figure 2, the microstructure of the 15-5 PH steel in the aged condition contains a small but significant fraction of austenite. The austenite islands are present as elongated islands with a thickness of 10-100 nm and a length up to 1 µm. They are mainly observed at the grains and laths boundaries of the martensitic structure. A systematic study of the orientation relationship between the martensite and these austenite islands has been carried out. It can be found in [18]. This study shows that the classical Kurdjumov-Sachs (KS) and Nishiyama-Wassermann (NW) are present in the microstructure [19–21].

Figure 3 shows X-ray diffractograms obtained both before and after the heat treatment. Small austenite peaks can be observed. The volume fraction of austenite after the ageing treatment was characterized according to the method of Tanaka and Choi [13]. In order to minimize possible texture effects on this evaluation, measurements were carried out in the three principal planes of the forged bar. They yielded very close values, averaging to 1.5% ± 0.34% (2σ) for the aged material. This value appears compatible with the ACOM measurements, although the area measured in this latter case is not sufficient to warrant a statistically valid value.

A quantitative evaluation of the austenite fraction before heat treatment is more challenging because of the lower intensity, but the presence of the peak indicates that austenite is already present. The above method gives 0.2% ± 0.34% of austenite.

The comparison of these two values shows that there is only a very small amount of retained austenite after the air quench and that the major part of this phase in the aged material has formed during the precipitation heat treatment at 505°C by reversion of martensite.

To further differentiate between the retained and reverted austenite, and evaluate the related spatial distribution of chemical species, an atom probe tip was measured along about 700 nm (corresponding to 48 million atoms). The material of this tip was further aged 2000h at 350°C after the ageing treatment at 505°C, in the framework of a study of long-term ageing in the 15-5 PH steel. However this additional heat treatment does not change the distribution

of solute at the scale that is discussed here [18] so that the results presented hereafter are applicable to the microstructure in the 505°C aged state.

Along the reconstructed APT volume, shown in Figure 4, several interfaces were crossed, including those surrounding austenite, as will be inferred from the local composition and microstructure. The local composition of the different encountered regions are given in Table 3.

The bottom of the analyzed volume is representative of the bulk material's microstructure with a dense distribution of nm-size Cu precipitates (defined by a 10 at% Cu iso-concentration surface), which will be detailed in subsequent paragraphs. This region clearly corresponds to the aged martensite. In the upper half of the Figure 4, a zone has a very peculiar microstructure, namely a Cu and Ni content very close to the nominal composition of the alloy (of the order of respectively 2 and 5 at%), with the Cu completely in solid solution. This last point means that Cu has not precipitated during the ageing treatment, so that we can infer that the material in this region was retained austenite in the as-quenched state, inheriting the nominal composition of the alloy from the mother austenite phase at high temperature.

This retained austenite is surrounded by two regions with a high Ni, Mn and C content. This high content of austenite stabilizers indicates that these zones consist of reverted austenite formed during the 505°C ageing treatment, involving a strong solute partitioning. Interestingly, these zones contain a high density of Cu precipitates, meaning that Cu precipitation probably occurred rapidly during the first stages of ageing, followed by the formation of the reverted austenite. A similar zone is observed in the lower half of the tip, however in this case not connected to retained austenite. Although the APT observation lacks a sufficient lateral extension to allow for conclusively determining the relationship between the different zones, these results suggest that reverted austenite can nucleate both on retained austenite and within the martensite (presumably on a lath boundary).

Finally, these reverted austenite regions are surrounded by regions of composition consistent with that of martensite, containing however a low density of Cu precipitates. A reasonable explanation for this low Cu content is diffusion to the reverted austenite during the ageing treatment, helping to form the high density of Cu precipitates observed in these regions.

3.3 Niobium carbides

The presence of niobium carbides is expected in this steel grade since niobium is added in order to trap the low level of carbon into carbides. These precipitates have been characterized in details in the 15-5PH grade by Habibi-Bajguirani [7,22,23]. In agreement with this work, we observed for the two studied conditions of the material spherical precipitates of approximately 300nm in diameter (Figure 5) identified by ACOM and selected area diffraction (not shown here) as niobium carbides. Their volume fraction is low and according to previous work [24], they are not expected to play a role in the mechanical behavior of the 15-5PH steel.

3.4 Copper precipitates

The copper precipitates appear during the heat treatment at 505°C subsequent to the quench. Their characteristics are particularly important because they play a prominent role in the control of the alloy's yield strength [7]. Apart from the austenitic regions or the martensite immediately surrounding these regions, their distribution appears to be homogeneous within the material as shown by APT in Figure 4 and confirmed by TEM in Figure 6. These observations also show the nearly spherical nature of the Cu precipitates, as well as an approximate

diameter of 5 nm. Such a near-spherical geometry is expected from a relatively low ageing temperature and time [7,25].

The atom probe characterization makes it possible to access more detailed information on the composition of the Cu precipitates, and of their surrounding. Figure 7 shows a 2 dimensional Ni composition map across a copper precipitate showing that the precipitates have a core-shell structure. A statistical characterization of this core-shell distribution of chemical species in the precipitates can be obtained by calculating a proxigram on all the interfaces defined by the 10 at%Cu iso-concentration surfaces [26]. The proxigram, averaged on 118 precipitates (70 closed and 48 opened isosurfaces) is shown in Figure 8. This proxigram shows a Cu content reaching 80 at% at the precipitate core. A focus on the minor concentration species (Figure 8b) evidences that a shell enriched in nickel and manganese, and in a lower extent in silicon, surrounds the precipitates. This type of core-shell structure with a shell rich in nickel and manganese has already been observed in different alloys containing these two elements [27–31]. According to the work of Isheim and co-authors the reason of the presence of such a shell is a decrease of the matrix/precipitate interface energy [31]. However one could also invoke a "snowplow effect" related to the expulsion of these chemical species from the precipitates during their formation [28,29]. In order to decide between these two possible causes for the Ni-enriched shell we compared the mean composition in the assembly precipitate + shell on one hand and in the surrounding matrix on the other hand. The first one is the ratio of all Ni atoms counted inside the isoconcentration surfaces used to obtain the proxigram in Figure 8 to all atoms inside these surfaces. The second one is the same ratio outside the isoconcentration surfaces. We obtain a mean concentration of 7.76% inside the assembly precipitates + shells and 5.48% in the matrix. The higher value of Ni concentration in both precipitates and shells is incompatible with a "snowplow effect" as the only mechanism of the shell formation; therefore some of the Ni atoms present in the shell have to come from the surrounding matrix. It is worth mentioning that this shell has a chemical composition that approaches that of the G phase [32], which is known to form during low-temperature ageing in this alloy family [33]. Therefore, it can be expected that the formation of the G phase may be favored in the area surrounding the Cu precipitates.

We obtain from the SAXS experiments the size distribution of the precipitates and, since we have characterized thanks to the APT technique the composition of the precipitates and of the surrounding matrix, we can also obtain their volume fraction [34]. For this purpose we assume that the precipitate size follows a lognormal distribution f(R) of spheres of median radius R_0 and size dispersion σ. We also assume that the precipitates are pure copper in a matrix with a composition of 80%at iron, 15%at chromium and 5%at nickel so we can calculate the electron density contrast $\Delta\rho$ between the precipitates and the matrix in order to deduce the volume fraction f_v from the integrated intensity Q_0, calculated from the integration of the scattered intensity I(q) at scattering vector q:

$$I(q) = \int_0^\infty KV^2 \left(\frac{sin(qR) - qRcos(qR)}{(qR)^3} \right)^2 f(R) dR \tag{3}$$

$$f(R) = \frac{1}{\sigma R\sqrt{2\pi}} exp\left(-\frac{1}{2} \left(\frac{ln\left(R/R_0\right)}{\sigma} \right)^2 \right) \tag{4}$$

$$Q_0 = \int_0^\infty I(q) q^2 dq = 2\pi^2 \Delta\rho^2 f_v (1 - f_v) \tag{5}$$

The fit of the precipitate size distribution to the SAXS intensity of the material aged at 505°C (Figure 9) provides a mean radius equal to 2.6nm with a relative standard deviation of 0.35. The calculation of the integrated intensity gives a volume fraction equal to 3.4%.

Further information on the precipitation kinetics was obtained by performing in-situ SAXS measurements during heat treatments. A first heat treatment was designed to mimic the industrial ageing treatment, with a relatively slow heating ramp of 5 K/min up to 505°C.

Figure 10 presents the evolution of the mean radius of the precipitates on the left-hand side and the one of the integrated intensity on the right-hand side. The time scale has been chosen such as t=0 corresponds to the time when the sample reached 500°C. The integrated intensity has not been translated into volume fraction because the aspect of its evolution led us to suspect that the contrast term $\Delta\rho^2$ may be changing during the experiment because of a change in the chemistry of the precipitates, especially in the very early stages. These graphs show a precipitate radius of about 0.5 nm at the end of the heating ramp. This radius can be considered as a nucleation radius. During subsequent ageing, the size progressively increases to reach 2 nm after 1h of ageing, this being compatible with the 2.6 nm radius measured at the end of the ageing treatment. As already mentioned, the evolution of the integrated intensity is more peculiar. Initially zero in the as-quenched state, it goes through a slight maximum at the end of the heating ramp, before reaching a plateau after 10 min of ageing. Assuming that this plateau corresponds to the same precipitate composition as characterized at the end of the ageing treatment discussed above, we calculated a volume fraction of 3.3%, very close to the volume fraction measured at the end of the 505°C ageing treatment (3.4%, see above).

As discussed by Osamura and his coauthors [28], the presence of the Ni and Mn enriched shell around the copper precipitates may be due to the sweeping out of these elements during the clusters growth and their transformation from BCC to FCC, leading to a change in the precipitates composition during the beginning of the heat treatment. This change in composition could result in a maximum in electron density contrast and thus explain the presence of the peak of integrated intensity at the very beginning of the ageing treatment. An alternative explanation could also be the redissolution at the end of the heating ramp of a small amount of the smaller precipitates formed during the ramp.

These results show that the Cu precipitates mainly nucleate during the heating ramp, so that the volume fraction is close to equilibrium at the beginning of the isothermal holding. The question then arises about the influence of the heating rate on the nucleation conditions and thus on the end microstructure. This was investigated by subjecting the as-quenched material to the same isothermal holding at 505°C with a much faster heating rate of 100 K/min. The results of Figure 10 show that this change of heating rate has no influence either on the precipitate size evolution or on the integrated intensity.

Another point of interest is the ageing temperature. The properties of the 15-5 PH alloy can be tailored by adjusting the ageing treatment. While the ageing treatment at 505°C studied here provides a material with a strength of 1200 MPa, a higher ageing temperature of 550°C has been used before, resulting in a strength level of 1070 MPa associated to a lower hardness and a higher ductility [7,9]. We investigated the precipitation kinetics at this 550°C ageing temperature with a heating rate of 5 K/min. The results in Figure 10 show that the precipitation kinetics followed during this heat treatment is qualitatively similar to that at 505°C. As expected, the nucleation size of precipitates is the same, since this precipitation stage corresponds to the heating ramp, which is the same between these two ageing temperatures. During the isothermal stage, the growth rate of the precipitate size is as

expected higher than at 505°C, resulting in a 0.5 nm radius difference after 1h of ageing. This difference is compatible with the measured size of about 5 nm [24,27] in the aged state at 550°C (1070 MPa grade 15-5 PH material). In parallel, the integrated intensity at the plateau is lower at 550°C as compared to that reached at 505°C, which is consistent with a higher level of Cu solubility in ferrite with increasing temperature.

3.5 Solute segregation at dislocations

During APT experiments we detected alignments of complex ions $NbN^{+/++}$ enriched zones (dark green surfaces on Figure 11). These alignments are characteristic of segregation of niobium and nitrogen along dislocations, allowing us to observe indirectly these crystal defects. In addition, we detected chromium-enriched zones (dark orange surfaces on Figure 11) together with these segregations of niobium and nitrogen. This is an indication of heterogeneous precipitation of chromium on dislocations. The core of these precipitates have a chromium concentration higher than 30%. Isoconcentration surfaces set at high chromium concentration (25%at) have a maximum size of a few nm. Although we did not perform APT measurements in the as-quenched state, this enrichment must have appeared during the ageing treatment, as the dislocations in martensite appear too fast during the quench to allow for substantial Cr diffusion. According to the work of Xiong et al. [35], the temperature of 505°C is close to the solvus line of the miscibility gap for the relatively low Cr content of our alloy. This can lead to a slow phase separation by nucleation and growth. The driving force being very low in this case, this phase separation is most likely to start heterogeneously on the dislocations.

In addition to this evaluation of the distribution of Cr atoms at the dislocations in the aged state, we evaluated the statistical spatial distribution of Cr in the ferrite matrix (i.e. away from dislocations) by two complementary methods performed on the same APT volumes, excluding the regions containing Cu precipitates or segregation on dislocations. First, we compared the distribution of compositions $M(C)$ measured by scanning a box of 100 atoms of base 1x1 nm through the APT reconstructed volume, and compared it to the theoretical distribution $R(C)$ for a random distribution of Cr atoms. The difference between the two distributions allows defining the degree of phase separation through the so-called V parameter [36–39].

$$V = \frac{\sum_C |M(C) - R(C)|}{\sum_C R(C)} \quad (6)$$

Figure 12a shows the distribution of Cr atoms in a slice of a reconstructed APT volume, and Figure 12b shows the experimental and random concentration distributions, whose difference result in a V parameter of 0.08. This low value is of the same order of magnitude, though higher, that the 0.02 V parameter measured by Danoix et al. in the unaged ferrite of a CF8M duplex stainless steel [40]. Another way to estimate the degree of phase separation is to calculate on the APT volume the radial distribution function (RDF) of Cr atoms [41]. The amplitude of the deviation from the value of 1 of this RDF represents the amplitude of fluctuations in solute content, and the extension of this deviation provides an estimate of the spatial extension of these fluctuations. This RDF is plotted for the aged material in Figure 12c. A small deviation is observed for sizes smaller than 0.5 nm, showing a low degree of very short range clustering of Cr atoms. Both analysis techniques thus agree in the fact that the Cr atom distribution in the aged state is nearly uniform away from dislocations, with a small tendency of clustering at very fine scale.

4 Conclusion

In the present work we have made a thorough characterization of the microstructure of the 15-5 PH steel in the precipitation-hardened state. Its main characteristics are as follows:

- The matrix is in majority a lath martensite, whose internal structure still contains a high density of dislocations despite the ageing treatment at 505°C.
- The material contains elongated islands of austenite mainly localized at grains and laths boundaries with a volume fraction of about 1.5%.
- The material contains approximately 3% volume fraction of finely dispersed small Cu precipitates (mean radius of 2.6 nm). Their core contains 80% Cu and they are surrounded by a shell rich in Ni, Mn and to a smaller extent in Si.
- The distribution of Cr atoms is not completely homogeneous, with the presence of small Cr-rich precipitates along dislocations together with segregations of Nb and N, and a small degree of phase separation in the matrix.

In addition, our study has evidenced the way in which this microstructure develops during the ageing treatment, from the as-quenched state, namely:

- In the as-quenched state the volume fraction of retained austenite is of the order of 0.5%. This retained austenite has the composition of the base material, and during ageing its Cu remains in solid solution. The reverted austenite that forms during ageing, however, is much richer in austenite formers (Ni, Mn, C), and is surrounded by a martensitic area nearly free of Cu precipitates.
- Precipitation of Cu occurs very rapidly during the heating ramp at 505°C, so that the equilibrium volume fraction is reached when reaching this temperature. Subsequently during isothermal holding, precipitate coarsening is observed. Changing the heating rate has no influence in the investigated range. When increasing the ageing temperature to 550°C precipitation coarsening occurs faster and a lower equilibrium volume fraction is reached.

Acknowledgments:

The authors acknowledge financial support from the CNRS-CEA “METSA” French network (FR CNRS 3507) for APT experiments conducted at the IM2NP platform and are grateful to Dr. Dominique Mangelinck for his help. The authors also acknowledge the French CRG beamline BM02 - D2AM at ESRF for SAXS beamtime. Aubert & Duval is thanked for providing the material of this study. This study was financially supported by the French ANR under contract ANR-2010-RMNP-017 (PREVISIA).

5 References

[1] K.H. Lo, C.H. Shek, J.K.L. Lai, Recent developments in stainless steels, Mater. Sci. Eng. R Rep. 65 (2009) 39–104. doi:10.1016/j.mser.2009.03.001.

[2] M. Abdelshehid, K. Mahmodieh, K. Mori, L. Chen, P. Stoyanov, D. Davlantes, et al., On the correlation between fracture toughness and precipitation hardening heat treatments in 15-5PH Stainless Steel, Eng. Fail. Anal. 14 (2007) 626–631. doi:10.1016/j.engfailanal.2006.03.001.

[3] P.J. Othen, M.L. Jenkins, G.D.W. Smith, High-resolution electron microscopy studies of the structure of Cu precipitates in α-Fe, Philos. Mag. A. 70 (1994) 1–24. doi:10.1080/01418619408242533.

[4] H.R. Habibi-Bajguirani, M.L. Jenkins, High-resolution electron microscopy analysis of the structure of copper precipitates in a martensitic stainless steel of type PH 15-5, Philos. Mag. Lett. 73 (1996) 155–162. doi:10.1080/095008396180786.

[5] R. Monzen, M.L. Jenkins, A.P. Sutton, The bcc-to-9R martensitic transformation of Cu precipitates and the relaxation process of elastic strains in an Fe-Cu alloy, Philos. Mag. A. 80 (2000) 711–723. doi:10.1080/01418610008212077.

[6] C.N. Hsiao, C.S. Chiou, J.R. Yang, Aging reactions in a 17-4 PH stainless steel, Mater. Chem. Phys. 74 (2002) 134–142. doi:10.1016/S0254-0584(01)00460-6.

[7] H.R. Habibi Bajguirani, The effect of ageing upon the microstructure and mechanical properties of type 15-5 PH stainless steel, Mater. Sci. Eng. A. 338 (2002) 142–159. doi:10.1016/S0921-5093(02)00062-X.

[8] M. Aghaie-Khafri, A. Zargaran, High temperature tensile behavior of a PH stainless steel, Mater. Sci. Eng. A. 527 (2010) 4727–4732. doi:10.1016/j.msea.2010.03.099.

[9] V. Anil Kumar, M.K. Karthikeyan, R.K. Gupta, G. Prakash, F, R. Kumar, et al., Aging Behavior in 15-5 PH Precipitation Hardening Martensitic Stainless Steel, Mater. Sci. Forum. 710 (2012) 483–488. doi:10.4028/www.scientific.net/MSF.710.483.

[10] D. Palanisamy, P. Senthil, V. Senthilkumar, The effect of aging on machinability of 15Cr–5Ni precipitation hardened stainless steel, Arch. Civ. Mech. Eng. 16 (2016) 53–63. doi:10.1016/j.acme.2015.09.004.

[11] O. Dmitrieva, D. Ponge, G. Inden, J. Millán, P. Choi, J. Sietsma, et al., Chemical gradients across phase boundaries between martensite and austenite in steel studied by atom probe tomography and simulation, Acta Mater. 59 (2011) 364–374. doi:10.1016/j.actamat.2010.09.042.

[12] H. Springer, M. Belde, D. Raabe, Bulk combinatorial design of ductile martensitic stainless steels through confined martensite-to-austenite reversion, Mater. Sci. Eng. A. 582 (2013) 235–244. doi:10.1016/j.msea.2013.06.036.

[13] M. Tanaka, C.S. Choi, The Effects of Carbon Contents and Ms Temperature on the Hardness of Martensitic Fe-Ni-C Alloys, Trans. ISIJ. 12 (1972) 16–25.

[14] F. Zhang, J. Ilavsky, G.G. Long, J.P.G. Quintana, A.J. Allen, P.R. Jemian, Glassy Carbon as an Absolute Intensity Calibration Standard for Small-Angle Scattering, Metall. Mater. Trans. A. 41 (2010) 1151–1158. doi:10.1007/s11661-009-9950-x.

[15] E.F. Rauch, M. Véron, Automated crystal orientation and phase mapping in TEM, Mater. Charact. 98 (2014) 1–9. doi:10.1016/j.matchar.2014.08.010.

[16] B. Gault, M.P. Moody, J.M. Cairney, S.P. Ringer, Specimen Preparation, in: At. Probe Microsc., Springer, Springer, 2012: pp. 71–110.

[17] H. Kitahara, R. Ueji, N. Tsuji, Y. Minamino, Crystallographic features of lath martensite in low-carbon steel, Acta Mater. 54 (2006) 1279–1288. doi:10.1016/j.actamat.2005.11.001.

[18] L. Couturier, Caractérisation des évolutions microstructurales de l'acier inoxydable martensitique à durcissement structural 15-5PH au cours du vieillissement thermique, phdthesis, Université de Grenoble, 2014. https://tel.archives-ouvertes.fr/tel-01127929/document (accessed June 22, 2015).

[19] G. Kurdjumow, G. Sachs, Über den Mechanismus der Stahlhärtung, Z. Für Phys. 64 (1930) 325–343. doi:10.1007/BF01397346.

[20] Z. Nishiyama, X-Ray Investigation of the Mechanism of the Transformation from Face-Centred Cubic Lattice to Body-Centred Cubic, Sci. Rep. Res. Inst. Tohoku Univ. 23 (1934) 637–673.

[21] G. Wassermann, Einfluss der α-γ-Umwandlung eines irreversiblen Nickelstahls auf Kristallorientierung und Zugfestigkeit, Arch. Für Eisenhüttenwes. 6 (1933) 347–351.

[22] H.R. Habibi Bajguirani, C. Servant, G. Cizeron, TEM investigation of precipitation phenomena occurring in PH 15-5 alloy, Acta Metall. Mater. 41 (1993) 1613–1623. doi:10.1016/0956-7151(93)90270-3.

[23] H.R. Habibi Bajguirani, Contribution à l'étude des transformations structurales se développant dans l'alliage 15-5 PH, en particulier les mécanismes de précipitations durcissantes à base de Cu, par microscopie électronique en transmission et diffusion des rayons X aux petits angles. Relations avec les caractéristiques mécaniques., Université Paris XI Orsay, 1993.

[24] E. Herny, Caractérisation mécanique et étude des mécanismes de vieillissement thermique et thermomécanique de l'acier inoxydable martensitique 15-5 PH, soudé par faisceau d'électrons, Institut National Polytechnique de Toulouse, 2006.

[25] M. Murayama, K. Hono, Y. Katayama, Microstructural evolution in a 17-4 PH stainless steel after aging at 400°C, Metall. Mater. Trans. A. 30 (1999) 345–353. doi:10.1007/s11661-999-0323-2.

[26] O.C. Hellman, J.A. Vandenbroucke, J. Rüsing, D. Isheim, D.N. Seidman, Analysis of Three-dimensional Atom-probe Data by the Proximity Histogram, Microsc. Microanal. 6 (2000) 437–444.

[27] G.M. Worrall, J.T. Buswell, C.A. English, M.G. Hetherington, G.D.W. Smith, A study of the precipitation of copper particles in a ferrite matrix, J. Nucl. Mater. 148 (1987) 107–114. doi:10.1016/0022-3115(87)90525-3.

[28] K. Osamura, H. Okuda, K. Asano, M. Furusaka, K. Kishida, F. Kurosawa, et al., SANS Study of Phase Decomposition in Fe-Cu Alloy with Ni and Mn Addition, ISIJ Int. 34 (1994) 346–354. doi:10.2355/isijinternational.34.346.

[29] P.J. Pareige, K.F. Russell, M.K. Miller, APFIM studies of the phase transformations in thermally aged ferritic FeCuNi alloys: comparison with aging under neutron irradiation, Appl. Surf. Sci. 94–95 (1996) 362–369. doi:10.1016/0169-4332(95)00398-3.

[30] M.K. Miller, B.D. Wirth, G.R. Odette, Precipitation in neutron-irradiated Fe–Cu and Fe–Cu–Mn model alloys: a comparison of APT and SANS data, Mater. Sci. Eng. A. 353 (2003) 133–139. doi:10.1016/S0921-5093(02)00679-2.

[31] D. Isheim, M.S. Gagliano, M.E. Fine, D.N. Seidman, Interfacial segregation at Cu-rich precipitates in a high-strength low-carbon steel studied on a sub-nanometer scale, Acta Mater. 54 (2006) 841–849. doi:10.1016/j.actamat.2005.10.023.

[32] T. Takeuchi, J. Kameda, Y. Nagai, T. Toyama, Y. Nishiyama, K. Onizawa, Study on microstructural changes in thermally-aged stainless steel weld-overlay cladding of nuclear reactor pressure vessels by atom probe tomography, J. Nucl. Mater. 415 (2011) 198–204. doi:10.1016/j.jnucmat.2011.06.004.

[33] S. Li, Y. Wang, X. Wang, F. Xue, G-phase precipitation in duplex stainless steels after long-term thermal aging: A high-resolution transmission electron microscopy study, J. Nucl. Mater. 452 (2014) 382–388. doi:10.1016/j.jnucmat.2014.05.069.

[34] F. DeGeuser, A. Deschamps, Precipitate characterisation in metallic systems by small-angle X-ray or neutron scattering, Comptes Rendus Phys. 13 (2012) 246–256. doi:10.1016/j.crhy.2011.12.008.

[35] W. Xiong, M. Selleby, Q. Chen, J. Odqvist, Y. Du, Phase Equilibria and Thermodynamic Properties in the Fe-Cr System, Crit. Rev. Solid State Mater. Sci. 35 (2010) 125–152. doi:10.1080/10408431003788472.

[36] D. Blavette, G. Grancher, A. Bostel, Statistical Analysis of Atom-Probe Data (I) : Derivation of some Fine-Scale Features from Frequency Distributions for Finely Dispersed Systems, J. Phys. Colloq. 49 (1988) 433–438. doi:10.1051/jphyscol:1988674.

[37] F. Danoix, P. Auger, D. Blavette, Hardening of Aged Duplex Stainless Steels by Spinodal Decomposition, Microsc. Microanal. 10 (2004) 349–354.

[38] E. Herny, P. Lours, E. Andrieu, J.M. Cloué, P. Lagain, Evolution of microstructure and impact-strength energy in thermally and thermomechanically aged 15-5 PH, Proc. Inst. Mech. Eng. Part J. Mater. Des. Appl. 222 (2008) 299–304. doi:10.1243/14644207JMDA190.

[39] T. Suzudo, Y. Nagai, D. Schwen, A. Caro, Hardening in thermally-aged Fe–Cr binary alloys: Statistical parameters of atomistic configuration, Acta Mater. 89 (2015) 116–122. doi:10.1016/j.actamat.2015.02.013.

[40] F. Danoix, P. Auger, Atom Probe Studies of the Fe–Cr System and Stainless Steels Aged at Intermediate Temperature: A Review, Mater. Charact. 44 (2000) 177–201. doi:10.1016/S1044-5803(99)00048-0.

[41] J. Zhou, J. Odqvist, M. Thuvander, P. Hedström, Quantitative Evaluation of Spinodal Decomposition in Fe-Cr by Atom Probe Tomography and Radial Distribution Function Analysis, Microsc. Microanal. 19 (2013) 665–675. doi:10.1017/S1431927613000470.

	Cr	Ni	Cu	Mn	Si	Mo	Nb	C	P	S	Fe
Min	14	3.5	2.5	0	0	0	0	0	0	0	bal.
Max	15.5	5.5	4.5	1	1	0.5	0.45	0.07	0.03	0.015	bal.

Table 1: Chemical composition of the 15-5PH alloy (wt%)

	a (Å)	θ (°)	F^2	P	L	e^{-2M}	R
$\alpha_{(110)}$	2.8765	26.11	969.7	12	0.99	0.958	19.9
$\gamma_{(111)}$	3.5949	25.55	4183.5	8	1.04	0.96	15.5

Table 2: Values used for the computation of the ratio R_α / R_γ

Element	Reverted austenite	Retained austenite	Depleted martensite	Average concentration of the alloy
Cr	14.24	15.24	14.90	15.85
Ni	16.13	5.31	4.10	4.65
Cu	0.40	2.09	0.14	2.61
Mn	1.72	0.97	0.73	0.81
Si	1.15	0.80	0.75	0.75
Mo	0.15	0.18	0.17	0.16
Nb	0.05	0.03	0.01	0.13
C	0.13	0.03	0.03	0.115

Table 3: composition (at%) of the different zones of the volume in Figure 4 determined in spherical ROIs.

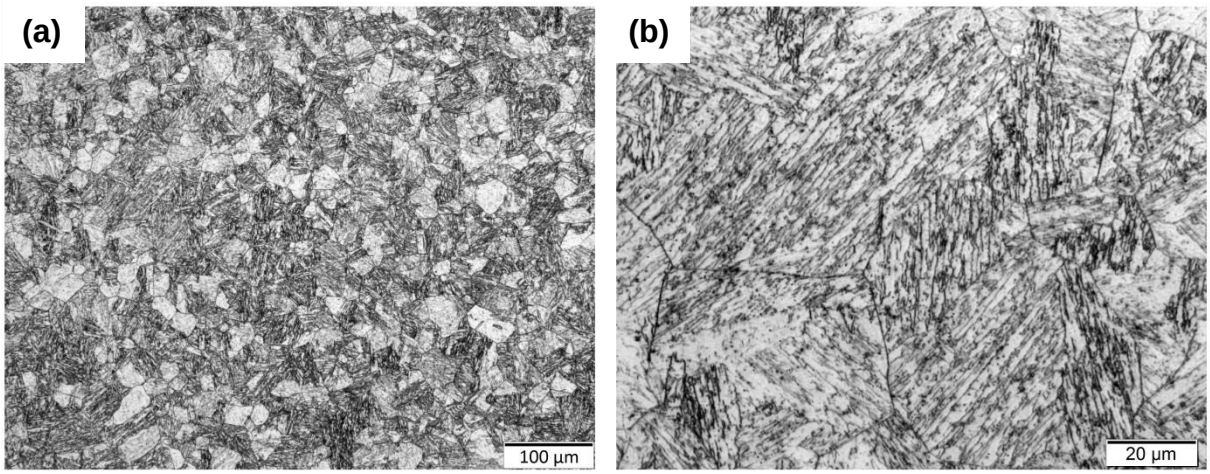

Figure 1: Optical micrographs of the 15-5PH alloy after the precipitation heat treatment showing the prior austenite grains (a) and the martensite laths they contain (b).

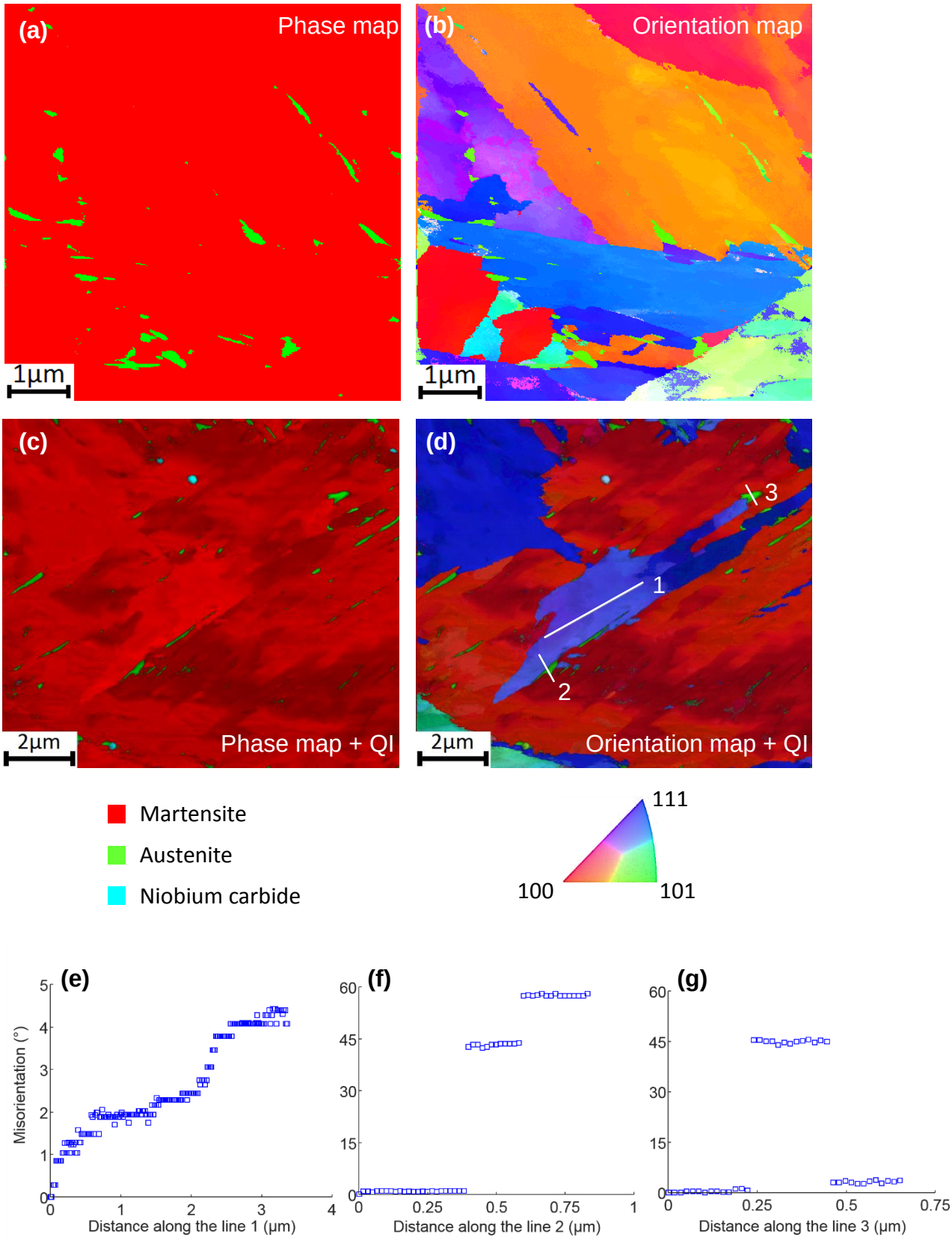

Figure 2: ACOM phase and orientation maps in the aged condition showing the microstructure of martensite, the spatial distribution of austenite. (a) and (b) phase and orientation maps of a first area. (c) and (d) phase and orientation maps of a second zone (quality index is superimposed to these two maps to illustrate the microstructure within the martensite laths). (e), (f) and (g) misorientation profiles for the linescans shown in figure (d), respectively within martensite, across a martensite grain boundary containing a martensite island, and across an austenite island embedded in martensite.

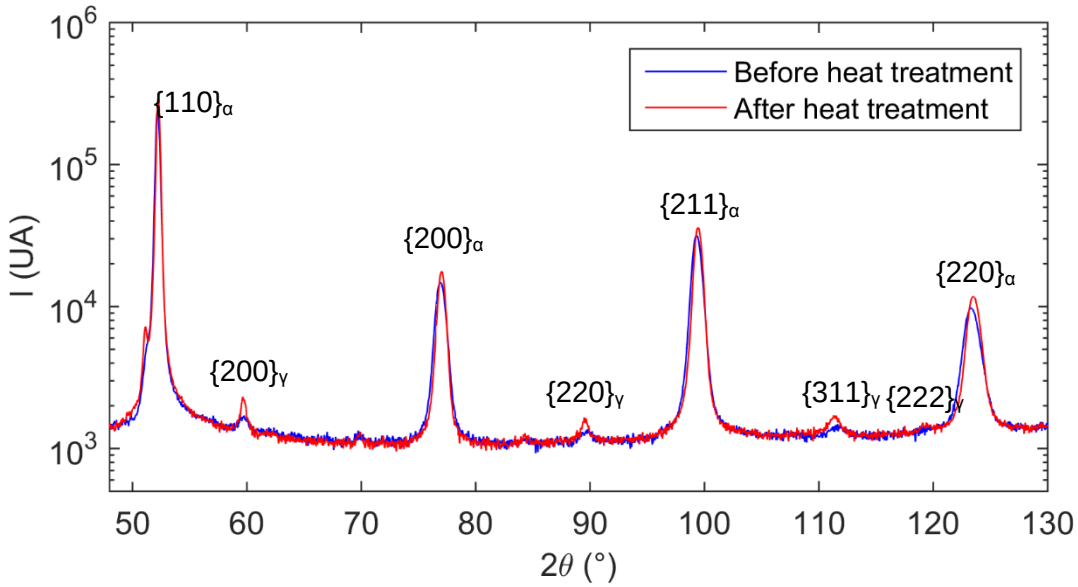

Figure 3: Comparison of the diffractograms before (as-quenched state) and after the ageing treatment at 505°C

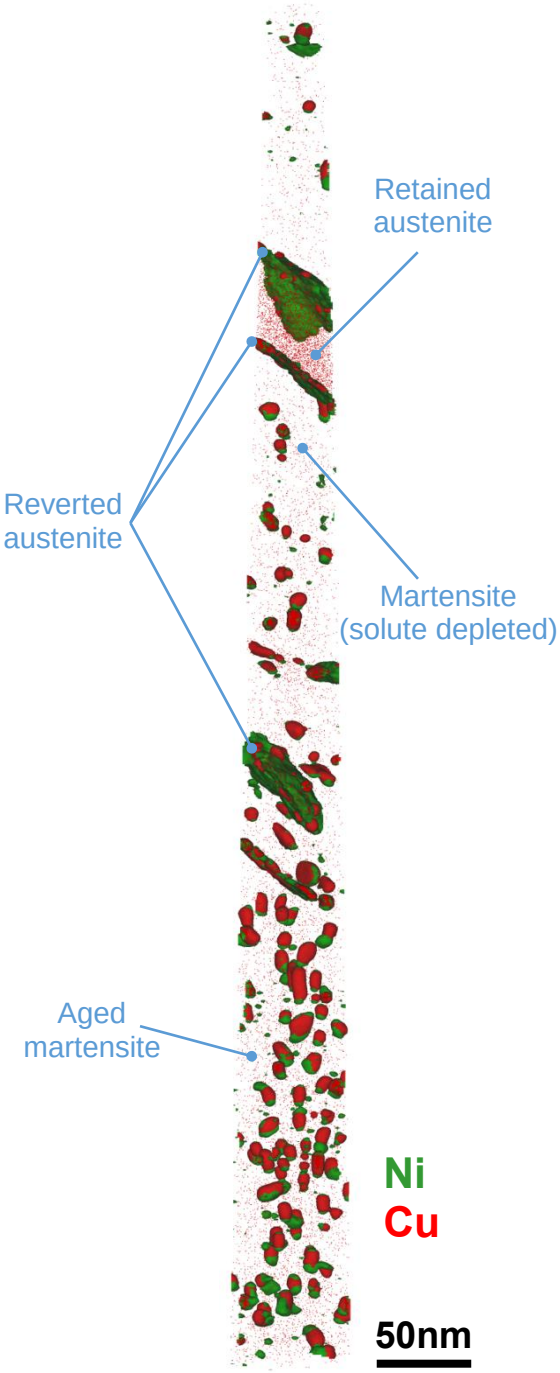

Figure 4: APT reconstructed volume of a sample aged 2000h@350°C. Only Ni (green) and Cu (red) atoms are represented as well as 10at% isoconcentration surface for the same elements. The different zones are discussed in the text.

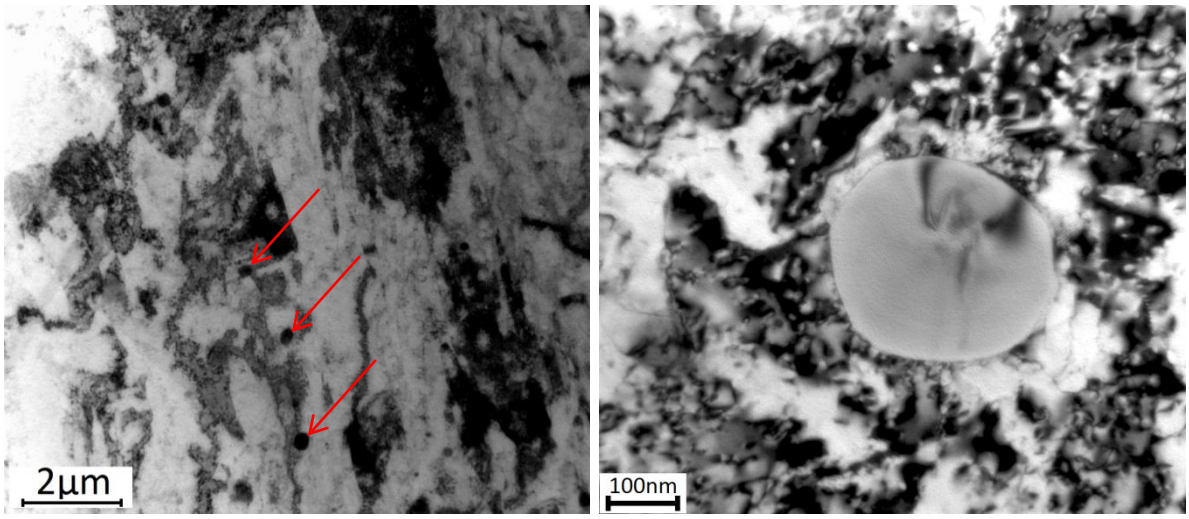

Figure 5: Bright field TEM micrographs showing spherical niobium carbides (arrows). Right hand side figure shows a larger magnification image of one carbide.

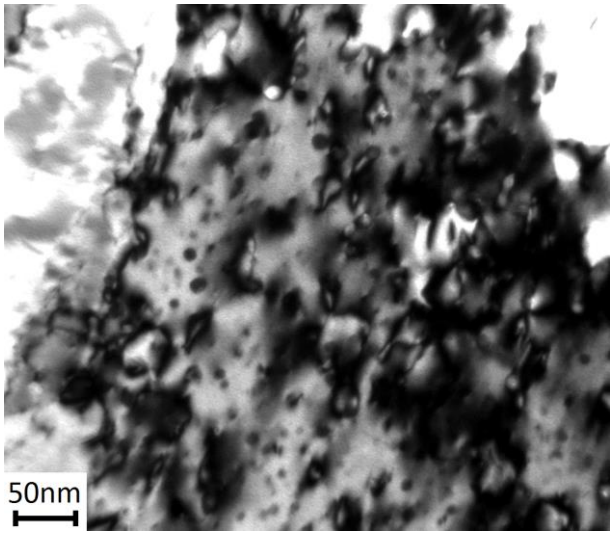

Figure 6: Bright field TEM micrograph of the aged material showing the distribution of the Cu precipitates

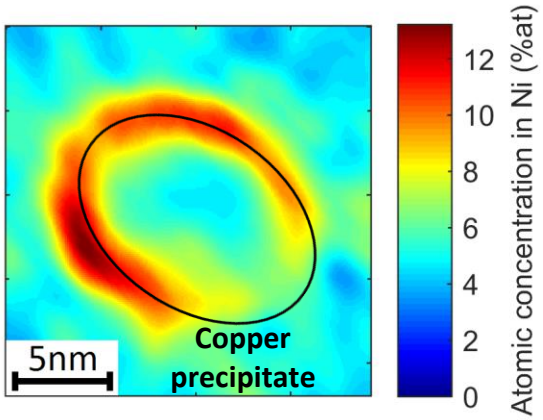

Figure 7: Ni concentration map on a cross section of a copper precipitate in an APT volume obtained don the aged material

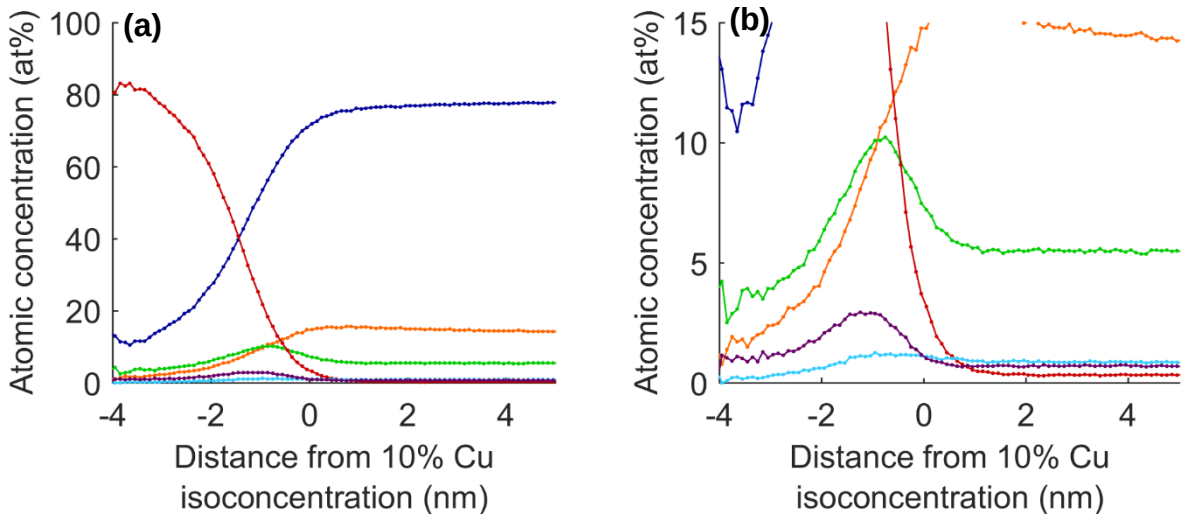

Figure 8: Proxigrams averaged on all the 10% Cu iso-concentration surfaces in the aged material, obtained from the APT volumes (a) and (b) differ by the concentration scale.

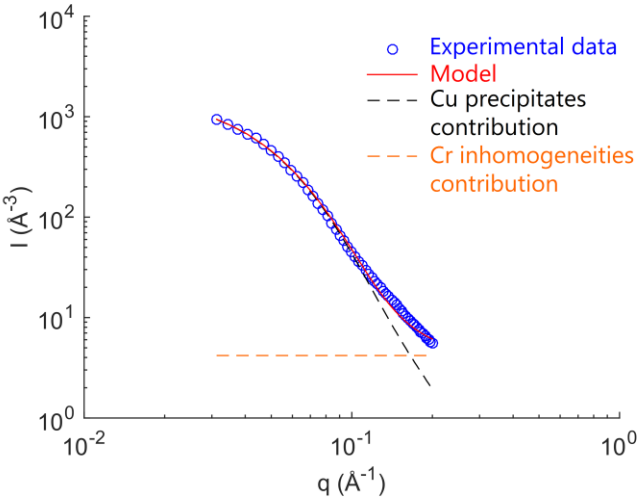

Figure 9: Measured SAXS intensity and fit by the intensity calculated from a log-normal distribution of spheres.

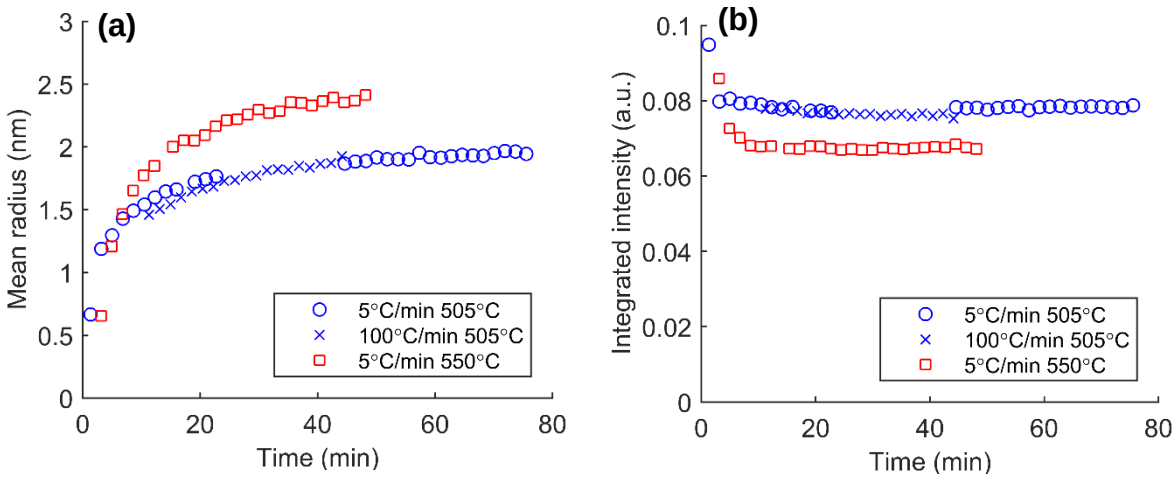

Figure 10: Evolution of the mean radius (a) and the volume fraction (b) of copper precipitates during heat treatments at 505°C and 550°C.

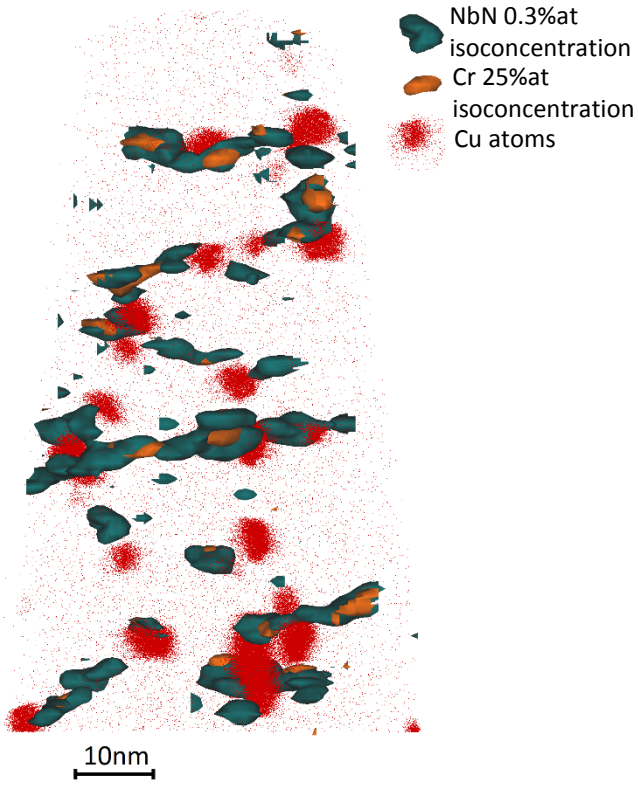

Figure 11: Alignments of NbN and Cr enriched zones in the precipitation hardened material

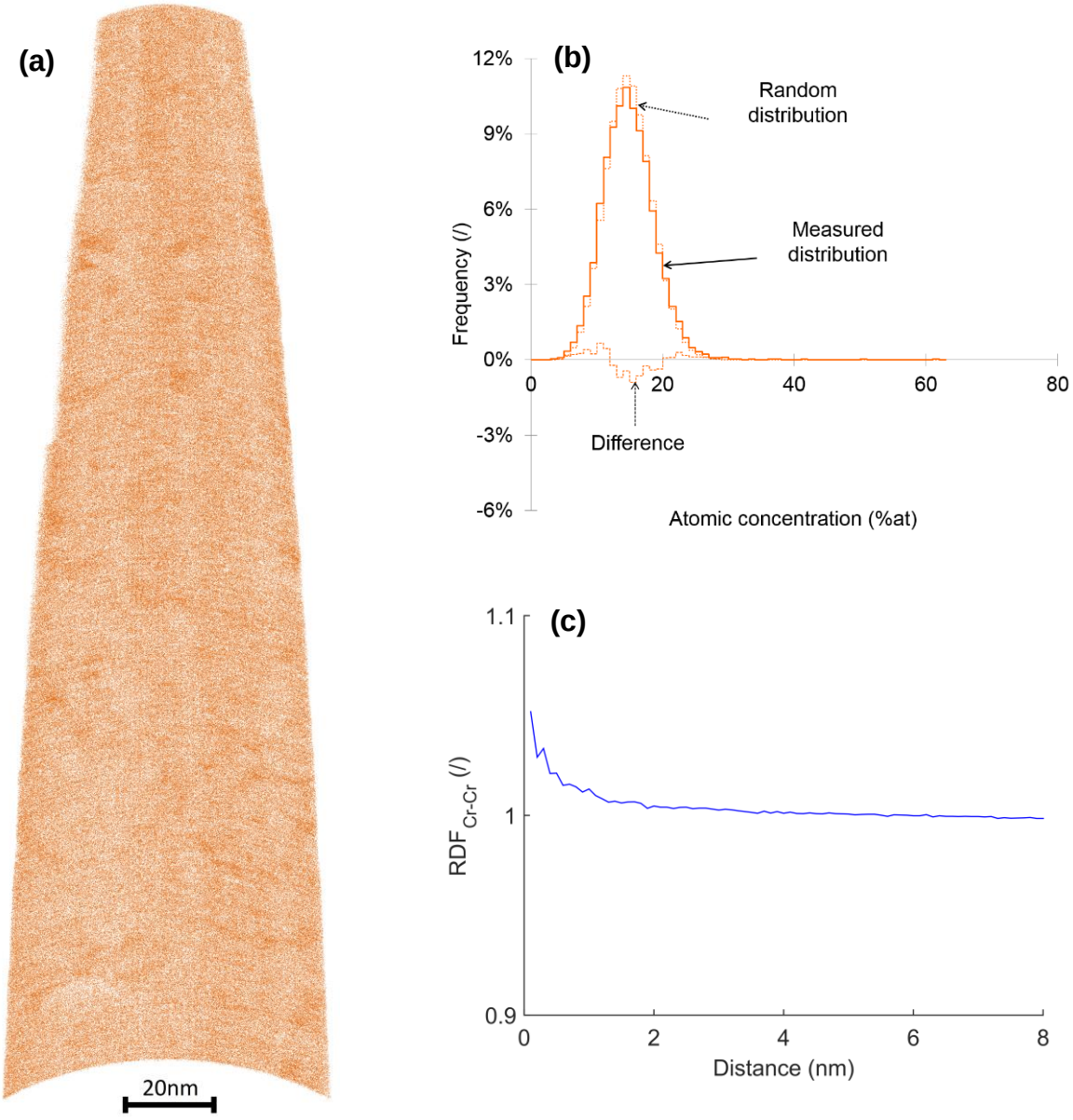

Figure 12: Distribution of the Cr atoms in a 15nm thick slice of the aged material APT volume (a) and the associated frequency distribution (b) and RDF (c) obtained for subvolumes containing only the matrix.